# Water waves overtopping over barriers

FRANCESCO GALLERANO[1], GIOVANNI CANNATA[1], MARCO TAMBURRINO[1],
SIMONE FERRARI[2], MARIA GRAZIA BADAS[2], GIORGIO QUERZOLI[2]

[1]Department of Civil, Constructional and Environmental Engineering
[1]"Sapienza" University of Rome
[1]Via Eudossiana 18 – 00184, Roma
[2]Department of Civil and Environmental Engineering and Architecture
[2]University of Cagliari
[2]Via Marengo 2 – 09123, Cagliari
ITALY
francesco.gallerano@uniroma1.it

*Abstract:* - A numerical and experimental analysis of the wave overtopping over emerged and submerged structures, is presented. An original model is used in order to simulate three-dimensional free surface flows. The model is based on the numerical solution of the motion equations expressed in an integral form in time-dependent curvilinear coordinates. A non-intrusive and continuous-in-space image analysis technique, which is able to properly identify the free surface even in very shallow waters or breaking waves, is adopted for the experimental tests. Numerical and experimental results are compared, for several wave and water depth conditions.

*Key-Words:* - water wave overtopping, free surface flows, numerical-experimental analysis, time-varying coordinates, image analysis

## 1 Introduction

The design of seawalls, breakwaters, sea dikes and, more generally, coastal structures, requires prediction of the wave overtopping over barriers [1].

In this work, a numerical and experimental study to investigate water waves overtopping over a structure is presented. Numerical models that are able to simulate the wave overtopping over a structure, have to incorporate the representations of wave transformation from deep to shallow water, wave breaking over variable bathymetry and wave run up on the structure. Models that solve depth-averaged equations, such as Nonlinear Shallow Water Equations (e.g. [2] and [3]) and Boussinesq Equations (e.g. [4], [5] and [6]), are widely used in this context [7]. Boussinesq Equations, which incorporate nonlinear and dispersive properties, are able to simulate both wave propagation and wave breaking (thanks to the shock-capturing property), but are not able to give a prediction of vertical distribution of variables, that is an essential property in order to represent phenomena present in the context of wave-coastal structure interactions, as undertow currents.

Another drawback of the models based on Boussinesq Equations is that they are not parameter free. In fact, in the shallow water zones, to properly simulate wave breaking, one has to switch from Boussinesq Equations to Nonlinear Shallow Water Equations, turning off dispersive terms; a criterion to define the zone in which there is the switch from one set of equations to the other, has to be defined.

In the context of domains with complex geometries, in order to overcome the limitations related to the use of Cartesian grids, numerical simulations can be carried out by using unstructured grids (e. g. [8], [9] and [10]) or boundary conforming grids. In this latter regard, many recent 3D models (e.g. [11] and [12]), map a time-varying physical domain into a fixed rectangular prismatic shape computational grid (the so-called σ-coordinate transformation). In these models, the kinematic and zero-pressure conditions at the free surface are assigned precisely, given the fact that the free surface position is at the upper computational boundary [13].

Models proposed by [13] and [14] simulate directly wave breaking, by incorporating into the σ-coordinates methodology shock-capturing methods. These models overcome the main drawback of the models that solve the Boussinesq Equations. In fact, in the σ-coordinates shock capturing models, no criterion has to be chosen to simulate the wave breaking phenomenon. In these models ([13], [14]),

the conserved variables are defined in a Cartesian system of reference and motion equations are solved on a coordinate system that includes a time-varying vertical coordinate.

In this work, we propose a new shock-capturing numerical model for the simulation of overtopping. In this model, the motions equations are expressed in an integral formulation on a boundary conforming time moving grid. The proposed formulation represents a generalization of the conservative formulation of the Navier-Stokes equations expressed in σ-coordinates.

In order to validate the numerical model, some laboratory experiments (with the same wave and obstacle parameters) have been carried out. The free-surface has been measured by means of the non-intrusive and continuous-in-space image analysis technique developed and tested by [15]. This technique is able to properly identify the wave free surface even in prohibitive situations for traditional resistive probes, such as very shallow waters and/or breaking waves.

The paper is structured as follows: in Chapter 2, we describe the proposed numerical model; in Chapter 3, we describe the experimental set-up; in Chapter 4, we present the results of a validation test for the numerical model and we compare numerical and experimental results for several overtopping tests; in Chapter 5, we present the conclusions of the study.

## 2 Numerical model

Let $(\xi^1, \xi^2, \xi^3, \tau)$ be a system of curvilinear coordinates, the transformation from Cartesian coordinates $(x^1, x^2, x^3)$ to the generalized curvilinear coordinates $(\xi^1, \xi^2, \xi^3)$ is:

$$\xi^1 = \xi^1(x^1, x^2, x^3, t) \quad \xi^2 = \xi^2(x^1, x^2, x^3, t) \quad \xi^3 = \xi^3(x^1, x^2, x^3, t) \tag{1}$$

Let $\vec{g}_l = \partial\vec{x}/\partial\xi^l$ be the covariant base vectors and $\vec{g}^l = \partial\xi^l/\partial\vec{x}$ the contravariant base vectors. The metric tensor and its inverse are defined by $g_{lm} = \vec{g}_l \cdot \vec{g}_m$ and $g^{lm} = \vec{g}^l \cdot \vec{g}^m$, with $(l, m = 1,2,3)$. The Jacobian of the transformation is given by $\sqrt{g} = \sqrt{det(g_{lm})}$.

Let $\Delta V(t)$ be a volume element defined by surface elements bounded by curves lying on the coordinate lines. We define the volume element in the physical space as:

$$\Delta V(t) = \Delta x^1 \Delta x^2 \Delta x^3 = \sqrt{g}\Delta\xi^1\Delta\xi^2\Delta\xi^3 \tag{2}$$

and the volume element in the transformed space as:

$$\Delta V^* = \Delta\xi^1\Delta\xi^2\Delta\xi^3 \tag{3}$$

Is to be noted that the volume element defined in eqn. (2) is time dependent, while the one defined in eqn. (3) is not. Similarly, we define the surface element which bounds $\Delta V$, in the physical space as $\Delta A(t) = \Delta x^\alpha \Delta x^\beta = \sqrt{g}\Delta\xi^\alpha\Delta\xi^\beta$ and in the transformed space as $\Delta A^* = \Delta\xi^\alpha\Delta\xi^\beta$ $(\alpha, \beta = 1,2,3$ are cyclic).

Let the total water depth be $H(x^1, x^2, t) = h(x^1, x^2, t) + \eta(x^1, x^2, t)$, where $h$ is the still water depth and $\eta$ is the free surface elevation. Let $(u_1, u_2, u_3)$ be the Cartesian components of the fluid velocity vector $\vec{u}$, and $(v_1, v_2, v_3)$ be the Cartesian components of the velocity vector of the control volume surfaces, $\vec{v}$. Our goal is to accurately represent the bottom and surface geometry and correctly assign the pressure and kinematics conditions at the bottom and at the free surface. A particular transformation from Cartesian to curvilinear coordinates, in which coordinates vary in time in order to follow the free surface movements, is:

$$\xi^1 = x^1; \quad \xi^2 = x^2; \quad \xi^3 = \frac{x^3 + h}{H}; \quad \tau = t \tag{4}$$

By means of the coordinate transformation defined by (4), the time-varying coordinates of the physical domain are basically mapped into a fixed coordinate system $(\xi^1, \xi^2, \xi^3)$, where $\xi^3$ spans from 0 to 1. In addition, the Jacobian of the transformation becomes $\sqrt{g} = H$. It has to be noted that, by means of the transformation defined by (4), the only non-zero component of the vector $\vec{v}$ is $v_3 = \partial x^3/\partial\tau$.

We define the cell averaged value (in the transformed space), respectively of the conservative variable $Hu_l$ and of the primitive variable $H$ (recalling that $H$ does not depend on $\xi^3$):

$$\overline{Hu_l} = \frac{1}{\Delta V^*}\int_{\Delta V^*} Hu_l d\xi^1 d\xi^2 d\xi^3 \tag{5}$$

$$\bar{H} = \frac{1}{\Delta A^*_{x^1x^2}}\int_{\Delta A^*_{x^1x^2}} H d\xi^1 d\xi^2 \tag{6}$$

where $\Delta A^*_{x^1x^2} = \Delta\xi^1\Delta\xi^2$ is the horizontal surface element in the transformed space.

By using eqn. (5), the integral form of the momentum equation over the volume $\Delta V$, expressed in the time dependent coordinate system defined in (4), can be written as follows (see [13]):

$$\begin{aligned}\frac{\partial\overline{Hu_l}}{\partial\tau} = &-\frac{1}{\Delta V^*}\sum_{\alpha=1}^{3}\left\{\int_{\Delta A^{*\alpha+}}[u_l(u_m-v_m)g_m^\alpha H]d\xi^\beta d\xi^\gamma - \int_{\Delta A^{*\alpha-}}[u_l(u_m-v_m)g_m^\alpha H]d\xi^\beta d\xi^\gamma\right\}\\ &-\frac{1}{\Delta V^*}\sum_{\alpha=1}^{3}\left\{\int_{\Delta A^{*\alpha+}}[G\eta g_m^\alpha H]d\xi^\beta d\xi^\gamma - \int_{\Delta A^{*\alpha-}}[G\eta g_m^\alpha H]d\xi^\beta d\xi^\gamma\right\}\\ &-\frac{1}{\Delta V^*}\frac{1}{\rho}\int_{\Delta V^*}\frac{\partial q}{\partial\xi^\alpha}g_m^\alpha H d\xi^1 d\xi^2 d\xi^3\\ &-\frac{1}{\Delta V^*}\sum_{\alpha=1}^{3}\left\{\int_{\Delta A^{*\alpha+}}[2\nu S_{lm}g_m^\alpha H]d\xi^\beta d\xi^\gamma - \int_{\Delta A^{*\alpha-}}[2\nu S_{lm}g_m^\alpha H]d\xi^\beta d\xi^\gamma\right\}\end{aligned} \quad (7)$$

where $\Delta A^{*\alpha+}$ and $\Delta A^{*\alpha-}$ indicate the boundary surfaces of the volume element $\Delta V^*$ on which $\xi^\alpha$ is constant and which are located at the larger and the smaller value of $\xi^\alpha$, respectively. Here the index $\alpha, \beta$ and $\gamma$ are cyclic. In eqn. (7) $G$ is the constant of gravity, $\rho$ is the fluid density, $q$ is the dynamic pressure, $\nu$ is the kinematic viscosity and $S_{lm}$ is the strain rate tensor.

By using eqn. (6), the integral form of the continuity equation over the water column, expressed in the time dependent coordinate system defined in (4), can be written as follows (see [13]):

$$\frac{\partial\overline{H}}{\partial\tau} + \frac{1}{\Delta A^*_{x^1x^2}}\sum_{\alpha=1}^{3}\left\{\int_{\Delta A^{*\alpha+}}[(u_m-v_m)g_m^\alpha H]d\xi^\beta d\xi^\gamma - \int_{\Delta A^{*\alpha-}}[(u_m-v_m)g_m^\alpha H]d\xi^\beta d\xi^\gamma\right\} = 0 \quad (8)$$

We assign the bottom and surface kinematic conditions as follows:

$$\int_{\Delta A^*_{x^1x^2(\xi^3=0)}}[u_l(u_m-v_m)g_m^3 H]d\xi^1 d\xi^2 = 0 \quad (9)$$

$$\int_{\Delta A^*_{x^1x^2(\xi^3=1)}}[u_l(u_m-v_m)g_m^3 H]d\xi^1 d\xi^2 = 0 \quad (10)$$

By using conditions (9) and (10) into eqn. (8), we obtain

$$\frac{\partial\overline{H}}{\partial\tau} + \frac{1}{\Delta A^*_{x^1x^2}}\int_0^1\sum_{\alpha=1}^{2}\left[\int_{\Delta\xi^{\alpha+}}Hu_\alpha d\xi^\beta - \int_{\Delta\xi^{\alpha-}}Hu_\alpha d\xi^\beta\right]d\xi^3 = 0 \quad (11)$$

in which $\xi^{\alpha+}$ and $\xi^{\alpha-}$ indicate the boundary lines of the surface element $\Delta A^*$ on which $\xi^\alpha$ is constant and which are located at the larger and the smaller value of $\xi^\alpha$ respectively. Eqn. (11) represents the governing equation that predicts the free surface motion.

Eqns. (7) and (11) represent the expression of the three dimensional motion equations as a function of the $\overline{Hu_l}$ and $\overline{H}$ variables in the coordinate system $(\xi^1, \xi^2, \xi^3, \tau)$. Eqns. (7) and (11) are numerically solved by means of a shock-capturing scheme that uses an approximate HLL Riemann solver. The solution is advanced in time by using a three-stage strong stability preserving Runge-Kutta (SSPRK) fractional step method. To take into account the effects of turbulence, we introduce a turbulent kinematic viscosity, estimated by means of the Smagorinsky sub grid model. Further details on the numerical scheme can be found in [13].

## 3 Experimental set-up

We carried out several laboratory tests, in a $21.00\ m$ long, $0.30\ m$ wide flume, with glass walls, a piston-type wave-maker and an absorbing beach to minimize the reflections. The adopted wave-maker is able to produce monochromatic regular wave trains. The wave period and the amplitude can be precisely assigned. More details can be found in [15].

A black painted trapezoidal obstacle of Perspex was used as bottom barrier. We employed still water depths ($0.29\ m$, $0.26\ m$ and $0.23\ m$): in the first experiment, the barrier is submerged, in the other two it is emerged. We seeded the water with a fluorescent dye, and we used a light sheet to illuminate the investigation area. We recorded the

images of the experiments by means of a digital video camera located orthogonally with respect to the investigation area: by means of this technique, the water appears bright in the recorded images, while the background and the barrier appear black. We carried out several experiment with different combinations of wave periods ($0.95\ s$ and $1.55\ s$), wave heights ($3.50\ cm$, $2.50\ cm$ and $1.00\ cm$) and still water levels.

We developed an image analysis technique in order to identify the free surface. By means of the developed technique, we overtake the drawbacks related to traditional probes, that are not able to properly work with very shallow water or breaking waves. Compared to traditional probes, the image analysis techniques have many advantages, as they are non-intrusive and quasi-continuous in space. For this reason, these techniques are used to measure, among the others, physical quantities such as object positions, pollutant concentrations [16] and/or flow velocities [17].

In the proposed procedure, the recorded images are smoothed by means of a median filter, and are binarized; the interface between bright and dark zones identifies the free surface. A pixel by pixel analysis of each column in the images is carried out, by means of the following procedure:

1. when a dark/bright interface is found, a certain number of successive pixels is checked;
2. if all the checked pixels are bright, the first of them is identified as belonging to the free surface; otherwise, the bright pixels are considered as a noise and the search for the free surface pixel continues;
3. when the free surface position is found at every column, we perform another median filter in order to smooth the line representing the free surface.

By this way, the free surface is identified even when the obstacle is emerged or in presence of breaking waves.

# 4 Results and discussion

## 4.1 Rip current test

In order to validate the proposed numerical model, we reproduce the laboratory experiment carried out by [18]. This test aims to verify the ability of the proposed model to reproduce nearshore currents induced by wave trains propagating over a spatially varying bottom.

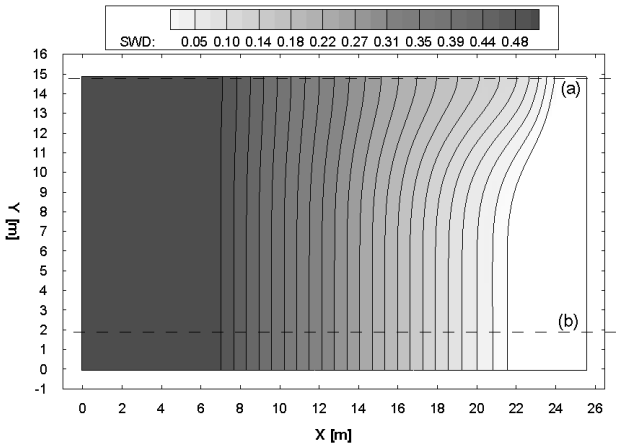


Fig. 1. Rip current test. Still water depth [m].

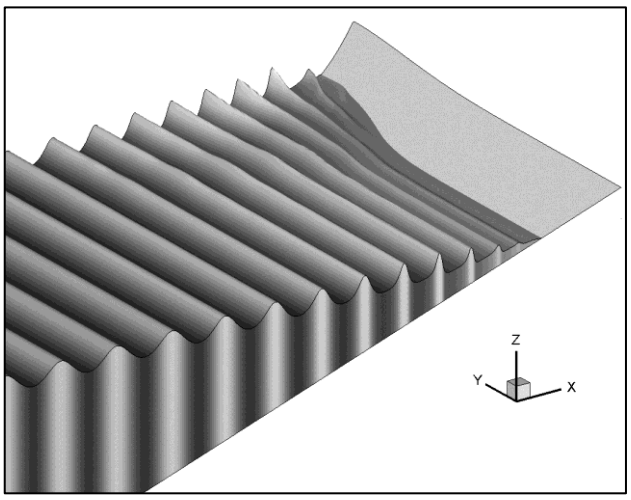


Fig. 2. Rip current test. Instantaneous free surface elevation 3D view.

The experimental set-up of the test carried out by [18] has the following features: a 30x30m basin, a plane sloping beach of 1:30 with a channel located along the centerline. Given that the bathymetry is symmetric with respect to the channel axis, the computational domain adopted for the numerical simulations reproduces only a half of the experimental domain (see fig 1). Reflective boundary conditions are imposed at the boundary that coincides with the channel axis. In Fig. 1 the two dashed lines indicate two significant cross sections: the vertical section along the channel axis (a) and the vertical section at the plane beach (b).

In this subsection, we show the results obtained by simulating a wave train generated in deep water ($X = 0\ m$) whose features are: wave period $T = 1.25\ s$, wave height $H = 0.07m$.

In Fig. 2 a three-dimensional view of the instantaneous wave field obtained by the proposed numerical model, is shown. Is to be noted that the wave shoaling and breaking occur nearer to the

beach in correspondence of the channel, due to the non-uniformity of the bottom.

Figs. 3 and 4 show the wave heights evolution along the sections (a) and (b), respectively. The good agreement between numerical and experimental results indicates that the model is able to reproduce the differences, in the shoaling and wave breaking phenomena, between the channel section (a) and the plane beach section (b).

The higher wave height in the channel is caused by an offshore directed current (rip current), opposite to the incoming waves. Fig. 5 shows the time-averaged flow velocity vectors near the bottom, obtained by the numerical simulation. As shown in Fig. 5, the rip current is generated by a longshore current, coming from the plane beach surf zone and turning offshore at the channel.

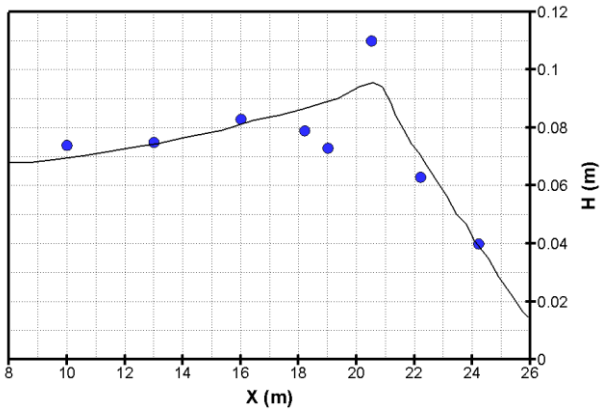


Fig. 3. Rip current test. Section (a). Solid line: mean wave height obtained by the proposed numerical model. Circles: experimental data from [18] for significant wave height $H_{1/3}$.

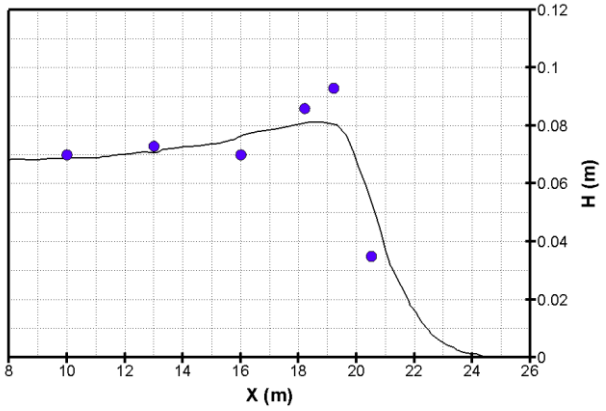


Fig. 4. Rip current test. Section (b). Solid line: mean wave height obtained by the proposed numerical model. Circles: experimental data from [18] for significant wave height $H_{1/3}$.

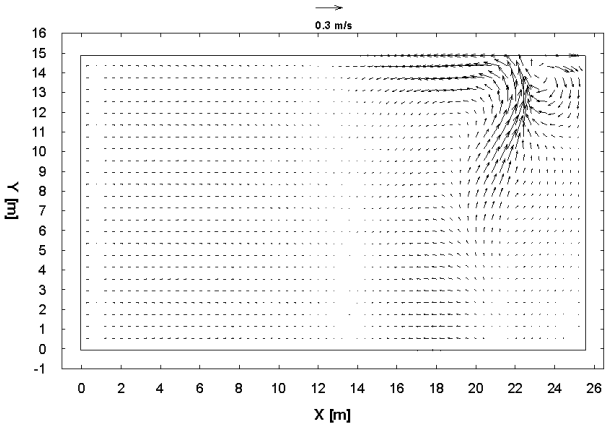


Fig. 5. Rip current test. Time-averaged flow velocity field near the bottom (one out of every 8 vectors).

## 4.2 Overtopping tests

To predict the behaviour of wave trains interacting with barrier in different configuration, three experimental tests have been carried out.

| Test | Still water depth [m] | Wave height [cm] | Wave period [s] |
|---|---|---|---|
| 1 | 0.23 | 3.5 | 1.55 |
| 2 | 0.26 | 1 | 1.55 |
| 3 | 0.29 | 2.5 | 0.95 |

For results analysis, phase-averaged free surface elevation is computed. In order to reproduce the experiments, we carried out several numerical tests with the proposed model.

### 4.2.1 Test 1

In Fig. 6 the comparison between numerical and experimental results for test 1, is shown. Is to be noted that the wave is partially able to pass over the barrier. Fig. 6a shows the wave in the run-up phase; the run-up phenomenon is reproduced with a good agreement between numerical and experimental results. In Figs. 6b and 6c, the wave propagation over the crest of the barrier is shown: the good agreement between numerical predictions and experimental measurements proves that the wave front propagation over flat bottoms is well predicted by the proposed numerical model. From Fig. 6d it can be deduced that even the simulated wave run-down is in agreement with the measured one. In Fig. 6e the wave trough at the offshore side of the barrier is shown, while Fig. 6f shows the beginning of the run-up phase: it must be noted that in these figures, there are some disturbances in the experimental measurements, at the onshore side of the barrier.

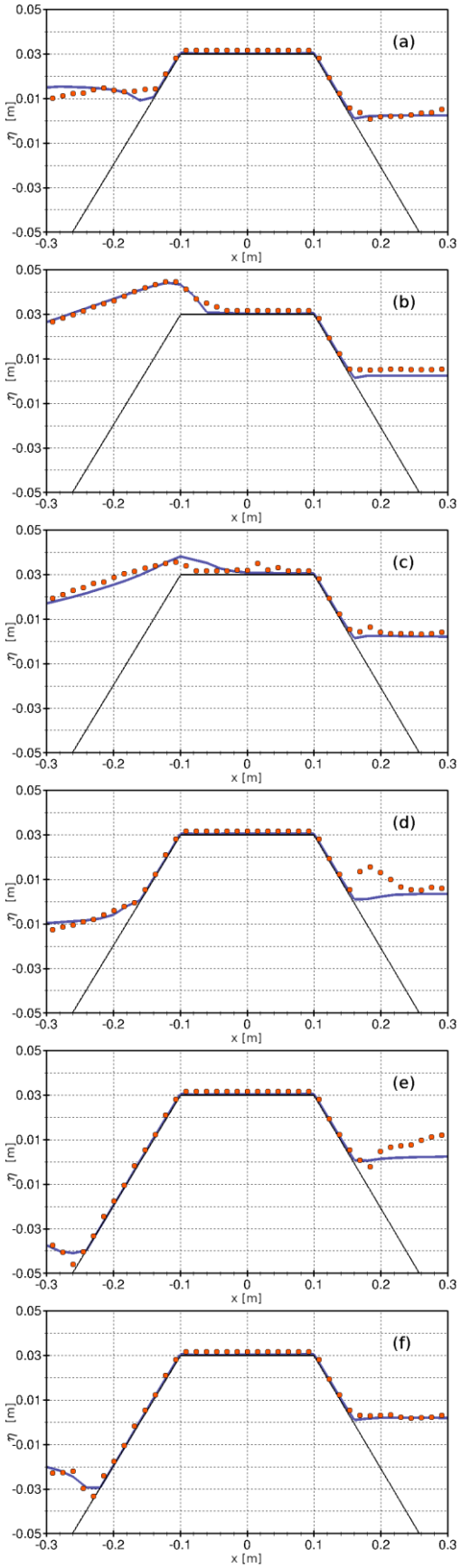


Fig. 6. Test 1. Phase-averaged free surface elevation [m] at t/T=0.0 (a), t/T=0.167 (b), t/T=0.333 (c), t/T=0.5 (d), t/T=0.667 (e), t/T=0.833 (f). Circles: experimental results. Blue line: numerical results.

### 4.2.2 Test 2

In Fig. 7 the comparison between numerical and experimental results for test 2, is shown. In this case, the wave propagates over the crest of the barrier with a very small water depth. Fig. 7a shows the wave run up over the offshore side of the barrier; as in the test 1, it can be seen that the run-up is well predicted and that the numerical results have a good agreement with the measurements. In Figs. 7b and 7c the wave propagating over the crest of the structure is shown; numerical and experimental results have a good agreement. Fig. 7d displays the wave that propagates over the inshore side of the barrier crest; is to be noted that in the experimental results the offshore side of the crest is shown dry. Figs. 7e and 7f show the run-down over the offshore side of the barrier; numerical and experimental results both well predict the phenomenon.

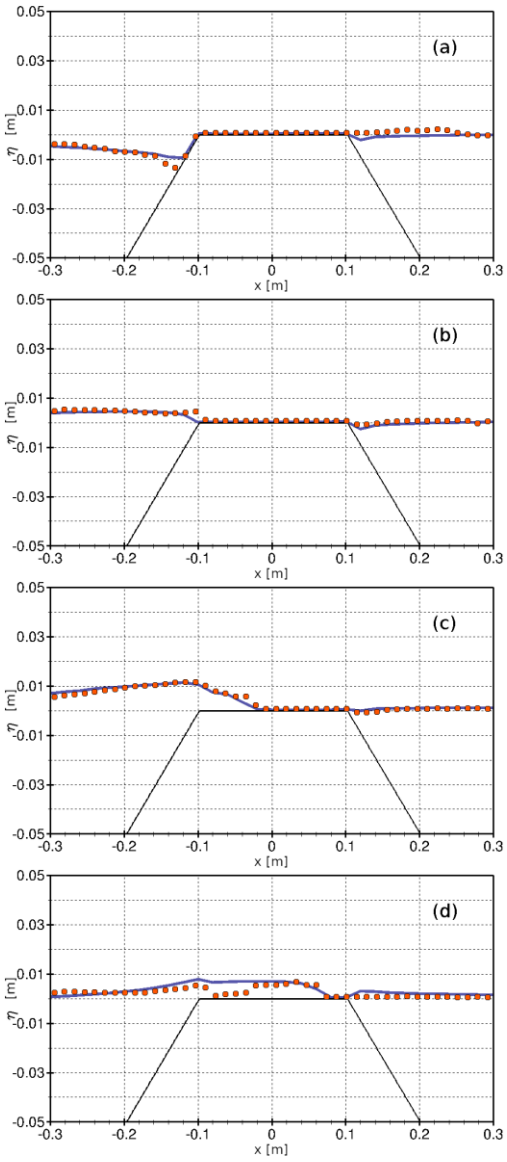

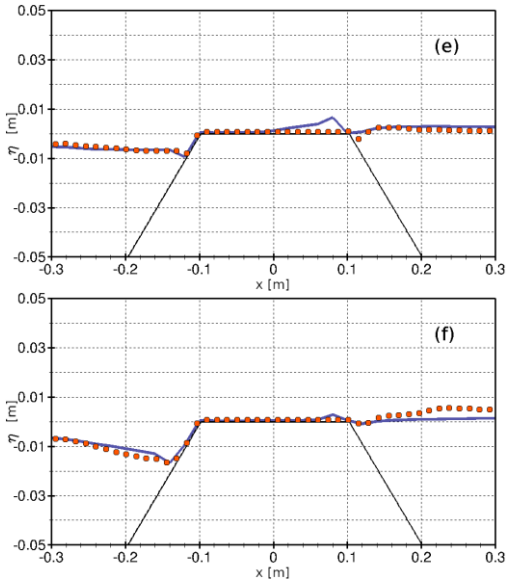


Fig. 7. Test 2. Phase-averaged free surface elevation [m] at t/T=0.0 (a), t/T=0.167 (b), t/T=0.333 (c), t/T=0.5 (d), t/T=0.667 (e), t/T=0.833 (f). Circles: experimental results. Blue line: numerical results.

### 4.2.3 Test 3

In Fig. 8 the comparison between numerical and experimental results for test 3, is shown. In this test, the barrier is completely submerged. In Figs. 8a and 8b, the wave crest propagating over the offshore side of the barrier is shown; there is a good agreement between numerical and experimental results. Figs. 8c and 8d show that the wave front propagation over the structure is well reproduced; the measured free surface is slightly higher than in the computed one. Figs. 8e and 8f display the wave crest passing the barrier; it must be noted that the wave front celerity is slightly higher in the numerical results than in the experimental ones.

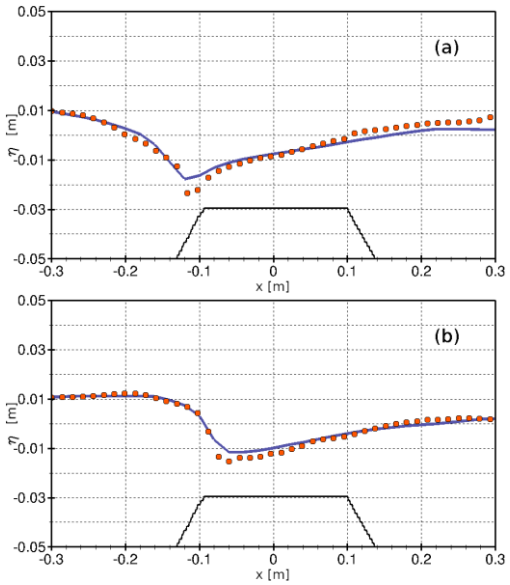


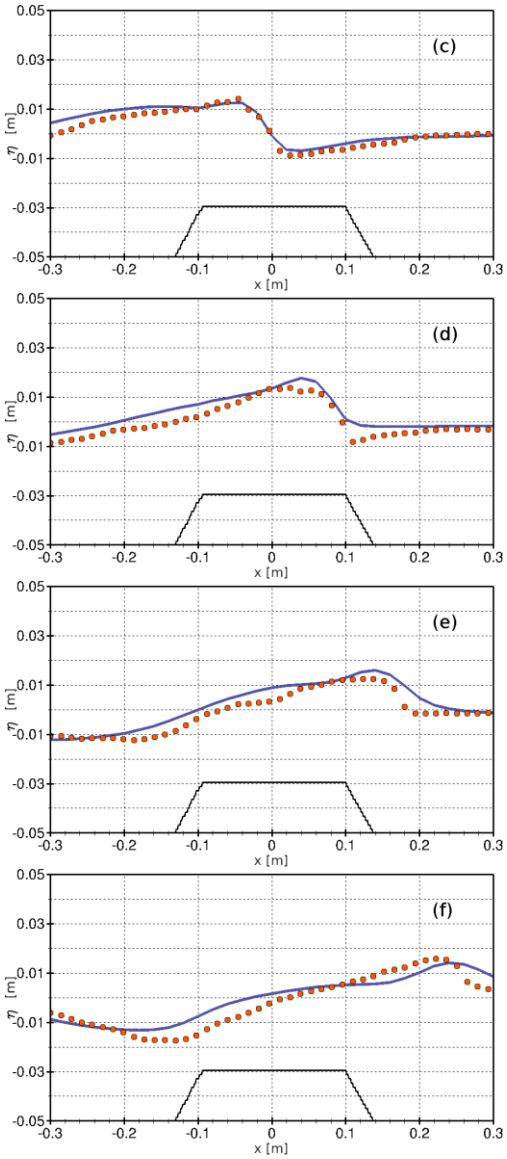


Fig. 8. Test 3. Phase-averaged free surface elevation [m] at t/T=0.0 (a), t/T=0.167 (b), t/T=0.333 (c), t/T=0.5 (d), t/T=0.667 (e), t/T=0.833 (f). Circles: experimental results. Blue line: numerical results.

## 4 Conclusion

A numerical and experimental analysis of the wave overtopping over structures phenomenon, has been presented. A new numerical model for the simulation of three-surface flows over barriers has been proposed. The proposed numerical model relies on an integral form of motion equations on a time-varying coordinate system. Several laboratory tests have been carried out, by adopting a non-intrusive and continuous-in-space image analysis technique.

Numerical and experimental results have been compared, for different wave and water depth conditions. From this comparison it can be seen that the proposed model is able to reproduce the features

of the phenomenon of the water waves overtopping over barriers.

*References:*

[1] Saville, T., *Laboratory data on wave run-up and overtopping on shore structures*, Tech. Rep. Tech. Memo. No. 64, U.S. Army, Beach Erosion Board, Document Service Center, Dayton, Ohio, 1955.

[2] Cannata, G., Lasaponara, F. & Gallerano, F., Non-linear Shallow Water Equations numerical integration on curvilinear boundary-conforming grids, *WSEAS Transactions on Fluid Mechanics*, Vol. 10, 2015, pp. 13–25.

[3] Cannata, G., Petrelli, C., Barsi, L., Fratello, F. & Gallerano, F., A dam-break flood simulation model in curvilinear coordinates, *WSEAS Transactions on Fluid Mechanics*, Vol. 13, 2018, pp. 60–70.

[4] Gallerano, F., Cannata, G. & Scarpone, S., Bottom changes in coastal areas with complex shorelines, *Engineering Applications of Computational Fluid Mechanics*, Vol. 11, No. 1, 2017, pp. 396–416.

[5] Gallerano, F., Cannata, G., De Gaudenzi, O. & Scarpone, S., Modeling Bed Evolution Using Weakly Coupled Phase-Resolving Wave Model and Wave-Averaged Sediment Transport Model, *Coastal Engineering Journal*, Vol. 58, No. 3, 2016, pp. 1650011-1–1650011-50.

[6] Cannata, G., Barsi, L., Petrelli, C. & Gallerano, F., Numerical investigation of wave fields and currents in a coastal engineering case study, *WSEAS Transactions on Fluid Mechanics*, Vol. 13, 2018, pp. 87–94.

[7] Tonelli, M. & Petti, M., Numerical simulation of wave overtopping at coastal dikes and low-crested structures by means of a shock-capturing Boussinesq model, *Coastal Engineering*, Vol. 79, 2013, pp. 75–88.

[8] Sørensen, O.R., Schäffer, H.A. & Sørensen, L.S., Boussinesq-type modelling using unstructured finite element technique. *Coastal Engineering*, Vol. 50, No. 4, 2003, pp. 181–198.

[9] Cioffi, F. & Gallerano, G., From rooted to floating vegetal species in lagoons as a consequence of the increases of external nutrient load: An analysis by model of the species selection mechanism. *Applied Mathematical Modelling*, Vol. 30, No. 1, 2006, pp. 10–37.

[10] Gallerano, F., Pasero, E. & Cannata, G., A dynamic two-equation Sub Grid Scale model. *Continuum Mechanics and Thermodynamics*, Vol. 17, No. 2, 2005, pp. 101–123.

[11] Cannata, G., Gallerano, F., Palleschi, F., Petrelli, C. & Barsi, L., Three-dimensional numerical simulation of the velocity fields induced by submerged breakwaters. *International Journal of Mechanics*, Vol. 13, 2019, pp. 1–14.

[12] Ma, G., Shi, F. & Kirby, J.T., Shock-capturing non-hydrostatic model for fully dispersive surface wave processes, *Ocean Modelling*, Vol. 43–44, 2012, pp. 22–35.

[13] Cannata, G., Petrelli, C., Barsi, L., Camilli, F. & Gallerano, F., 3D free surface flow simulations based on the integral form of the equations of motion, *WSEAS Transactions on Fluid Mechanics*, Vol. 12, 2017, pp. 166–175.

[14] Gallerano, F., Cannata, G., Lasaponara, F. & Petrelli, C., A new three-dimensional finite-volume non-hydrostatic shock-capturing model for free surface flow, *Journal of Hydrodynamics*, Vol. 29, No. 4, 2017, pp. 552–566.

[15] Ferrari, S., Badas, M.G., & Querzoli, G., A non-intrusive and continuous-in-space technique to investigate the wave transformation and breaking over a breakwater, *EPJ Web of Conferences*, Vol. 114, art. No. 02022, 2016.

[16] Besalduch, L.A., Badas, M.G., Ferrari, S. & Querzoli, G., On the near field behavior of inclined negatively buoyant jets. *EPJ Web of Conferences*, Vol. 67, art. No. 02007, 2014.

[17] Garau, M., Badas, M.G., Ferrari, S., Seoni, A. & Querzoli, G., Turbulence and Air Exchange in a Two-Dimensional Urban Street Canyon Between Gable Roof Buildings, *Boundary-Layer Meteorology*, Vol. 167, No. 1, 2018, pp. 123–143.

[18] Hamm, L., Directional nearshore wave propagation over a rip channel: an experiment, *Proceedings of the 23rd International Conference of Coastal Engineering*, 1992.